# Chapter 5

# Magnetic state of the martensite phase in $Ni_2Mn_{1.4}In_{0.6}$ magnetic shape memory alloy: A muon spin relaxation study

In this chapter, we explore the magnetic state within the paramagnetic gap region of the martensite phase in $Ni_2Mn_{1.4}In_{0.6}$ magnetic shape memory alloy using the muon spin relaxation ($\mu$SR) technique. Additionally, pair distribution function analysis is performed to identify a local martensite phase within the austenite phase.

## 5.1 Introduction

Ni-Mn-based magnetic shape memory alloys (MSMAs) have garnered significant attention in recent decades due to their widespread applications such as magnetically actuated devices [1], energy conversion [2], and spintronics [3]. This interest is driven by their unique multifunctional properties, including the shape memory effect [4], magnetocaloric effect [5, 6], large magnetoresistance [7], giant Hall effect [8], and exchange bias effect [9]. In temperature-dependent magnetization ($M(T)$) measurements, these MSMAs undergo a magneto-structural transition at their martensite phase transition ($T_M$) [10]. The high-temperature phase of these MSMAs is the high-symmetry austenite (cubic) phase, and below $T_M$, they transform into the low-symmetry tetragonal/orthorhombic/monoclinic phase [11, 12]. In the austenite phase, these alloys undergo a magnetic transition from the paramagnetic (PM) phase to the ferromagnetic (FM) phase at the Curie temperature ($T_C$). The FM behaviour arises from the Ruderman-Kittel-Kasuya-Yosida (RKKY) interaction between Mn atoms, facilitated by conduction electrons [13]. On cooling forward from the austenite phase, magnetization sharply decreases below the $T_M$, leading to a weak magnetic phase due to the loss of magnetic order [14]. With further cooling, another magnetic transition occurs in the martensite phase, known as the Curie temperature in the martensite phase ($T_C^M$) [11, 15–20]. The temperature range between $T_M$ and $T_C^M$, characterized by low magnetization, is referred to as so-called PM gap [15, 18, 19].

For most technological applications, MSMAs should have $T_M < T_C$. This ensures that during the martensite phase transition, the materials retain a magnetically ordered state in austenite phase [21]. The physical properties of the MSMAs are directly linked to the magnetoelastic coupling at the martensite transition, which encourages the elaborated study of

the magnetic interactions in the martensite phase [3, 22, 23]. In the Ni-Mn-X (X=Sb, Sn and In) based MSMAs, antiferromagnetic (AFM) correlations are reported in their martensite phase using first principle calculation [10, 24–28]. Monte Carlo simulations indicate that AFM interactions occur between Mn atoms present at inter-sublattice sites [24, 27] and the increasing AFM correlations contribute to the reduction of magnetization in the martensite phase. Several experimental observations report that leading AFM interactions decrease the magnetization below the $T_M$ [11, 13, 14, 29–33]. Neutron polarization analysis experiments reveal the AFM state in the martensite phase and conclude that the increase in the antiferromagnetic ordering is strongly associated to the Mn-Mn bonding in Mn-rich Ni-Mn-X (X=Sb, Sn and In) based MSMAs alloys and similar compositions [17]. Other reports, based on Mössbauer experiments, suggest that the martensite phase of Fe-doped Ni-Mn-Sn [34] and Fe-doped Ni-Mn-In [35] corresponds to the PM phase. Additionally, the muon spin relaxation technique has confirmed that the low-temperature martensite phase of $Ni_2Mn_{1.4}Sn_{0.6}$ is PM phase [21]. The extensive literature questioning the true magnetic nature of the martensite phase within the so-called PM gap remains a topic of ongoing debate.

The $Ni_2Mn_{1.4}In_{0.6}$ (and close stochiometric) composition is important among the other Ni-Mn-In based MSMAs due to its technological properties such as the giant barocaloric effect [36], reversible magnetocaloric effect [37, 38], elastocaloric effect [39], superelastic stability [40], colossal negative magnetoresistance [41], anomalous and topological Hall and Nernst effects [41], large exchange bias [42], and zero field skyrmionic phase [3] etc. These technologically important properties are closely related to the austenite-martensite phase transition, and crystal structure of the martensite phase of $Ni_2Mn_{1.4}In_{0.6}$ and related compositions [36, 38, 39, 43]. Although the crystal structure in the martensite phase has been established as 3M modulated [44, 45], the magnetic structure is still unresolved and a matter of debate [44, 46]. Neutron diffraction is an effective method for examining magnetic structures and has been utilized to study the magnetic structure of Ni-Mn-based MSMAs, which exhibit tetragonal or orthorhombic structures in the martensite phase [18, 21, 47, 48]. However, neutron diffraction measurements could not resolve the magnetic

structure of the so-called PM gap in the martensite phase of the $Ni_2Mn_{1.4}In_{0.6}$ due to its complex modulated crystal structure [46] although an indication of an antiferromagnetic arrangement of Mn spins is found at lower temperature [44]. Recently, the $\mu$SR technique emerged as a very powerful tool to understand complex magnetic structures [49–51] and has also been used for Ni-Mn-based MSMAs [21, 52]. $\mu$SR technique is a local probe method used to investigate the magnetic properties and validate the magnetic signature of the materials. Its unique ability lies in detecting very low magnetic moment due to its large magnetic moment.

In the present study, we examine the magnetic structure of the $Ni_2Mn_{1.4}In_{0.6}$ MSMA composition using zero-field muon spin relaxation ($\mu$SR) measurements. Our study reveals the dynamic relaxation of muon polarization near the magnetic transition temperature, which aligns with the temperature-dependent magnetization plot. The $\mu$SR asymmetry signal distinguishes between ordered and disordered (PM) spin states. The low asymmetry values obtained between $T_M$ and $T_C^M$ confirm that the magnetic state in the so-called PM gap is an ordered magnetic phase. The temperature-independent higher asymmetry values above $\sim 395$ K indicate the PM nature of the high-temperature phase. The reduced asymmetry values, even above the $T_C$, are explained using pair distribution function (PDF) data analysis and the existence of a local martensite phase. Our results provide a clear understanding of the magnetic state in the so-called PM gap of $Ni_2Mn_{1.4}In_{0.6}$ MSMA and suggest a method for determining the magnetic states of complex modulated crystal structures.

## 5.2 Experimental details

A polycrystalline compound of $Ni_2Mn_{1.4}In_{0.6}$ was prepared via arc melting technique, using high-purity constituent elements (purity $> 99.99\%$) in an argon atmosphere [6, 53, 54]. The synthesis procedure involved six melting cycles. During each cycle, the sample was flipped to ensure uniform composition.Subsequently, the sample was sealed in an evacuated quartz ampoule, annealed at 973 K for 3 days, and quenched in an ice-water mixture.

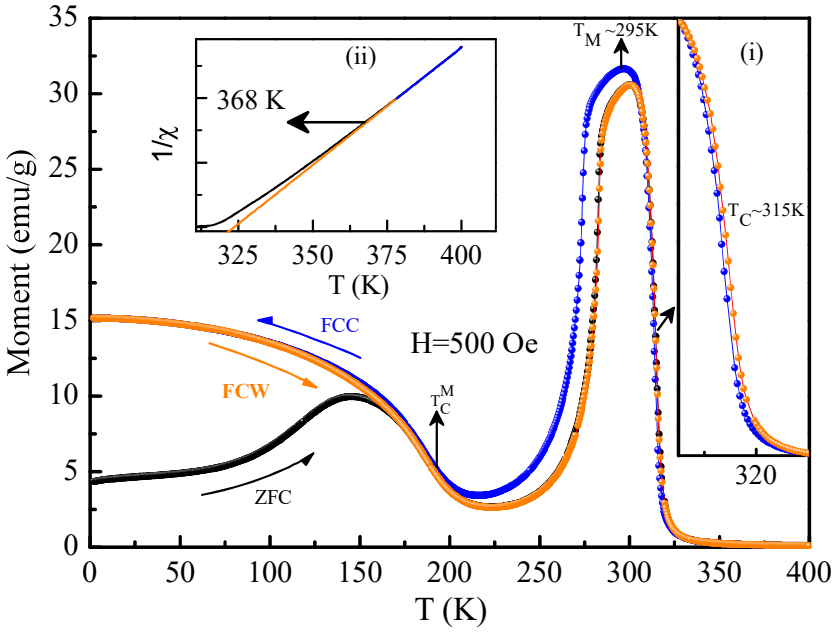


Figure 5.1: Magnetization as a function of temperature ($M(T)$) for zero-field cooling (ZFC), field-cooled cooling (FCC), and field-cooled heating (FCW) with a 500 Oe external magnetic field. Inset (i) magnified view of the $M(T)$ plot around $T_C$. (ii) magnified view of $1/\chi$ vs $T$ plot at high temperature [44].

A portion of the annealed bulk sample was then crushed into fine powder to prepare it for characterization. The powder was then subjected to annealing under vacuum conditions, a step designed to eliminate any residual stress-induced effects [55–57]. $M(T)$ measurements were performed using a superconducting quantum interference device (SQUID) magnetometer with a low magnetic field of 500 Oe. Zero field (ZF) $\mu$SR experiments were performed at the ISIS Neutron and Muon Facility using EMU spectrometer [58]. The sample was placed on a high-purity (99.999%) silver sample holder, secured with GE varnish to reduce background interference. Measurements were performed in zero field across a temperature range of 421 K to 117 K. Synchrotron X-ray powder diffraction (SXRPD) measurements were conducted at the P02.1 beamline at PETRA-III, DESY, Germany, offering low background, high intensity, and high resolution. The measurements utilized X-rays with a wavelength ($\lambda$) of 0.2071 Å. Temperature-dependent PDF data were also collected at the same beamline with a maximum instrumental Q-value (Qmax) of 20.73 $Å^{-1}$, covering a temperature range from 350 K to 100 K in 10 K intervals.

## 5.3 Results and discussion

### 5.3.1 Magnetization

The $M(T)$ data of $Ni_2Mn_{1.4}In_{0.6}$ is measured at a field of 500 Oe under Zero-field-cooled (ZFC), field-cooled cooling (FCC), and field-cooled warming (FCW) protocols. (shown in Fig. 5.1) [44]. At elevated temperatures in the austenite phase, the material is in the PM state and undergoes a magnetic transition from PM to FM phases at $T_C$ ($\sim$ 315 K). As the temperature decreases, the magnetic transition is accompanied by a magnetostructural transition from the austenite to the martensite phase at $T_M \sim 295$ K. At $T_M$, a sharp decrease in magnetization occurs, reflecting the disruption of magnetic order in the martensite phase. Upon further cooling within the martensite phase, another broad magnetic transition occurs around $T_C^M \sim 190$ K. The divergence between ZFC and FCC plots below the second magnetic transition indicates the existence of competing FM and AFM interactions. Inset (i) of Fig. 5.1 displays the zoomed view of the thermal hysteresis at around $T_C$. The origin of the hysteresis may be due to the presence of the local martensite phase in the cubic phase at high temperatures. Inset (ii) represents the $1/\chi$ plot vs $T$, indicating a ferromagnetic correlation at higher temperatures above $T_C$.

### 5.3.2 Muon spin relaxation analysis

In the $\mu$SR experiment, spin-polarized muons are introduced into the sample, and their polarization relaxes in response to the local magnetic field at the implantation site until they decay (with a lifetime of 2.2 $\mu$s). The implanted muons interact with the sample and decay into positrons, an elementary particle. These positrons are emitted predominantly in the forward direction, aligned with the muon spin, and also in the backward direction [59, 60]. In the zero-field (ZF) measurement, the positrons emitted in the forward direction are counted by a detector aligned with the muon spin direction, while the positrons emitted in the backward direction are counted by a detector positioned opposite to the initial muon spin direction [61]. These forward and backward detector count the emitted positrons as

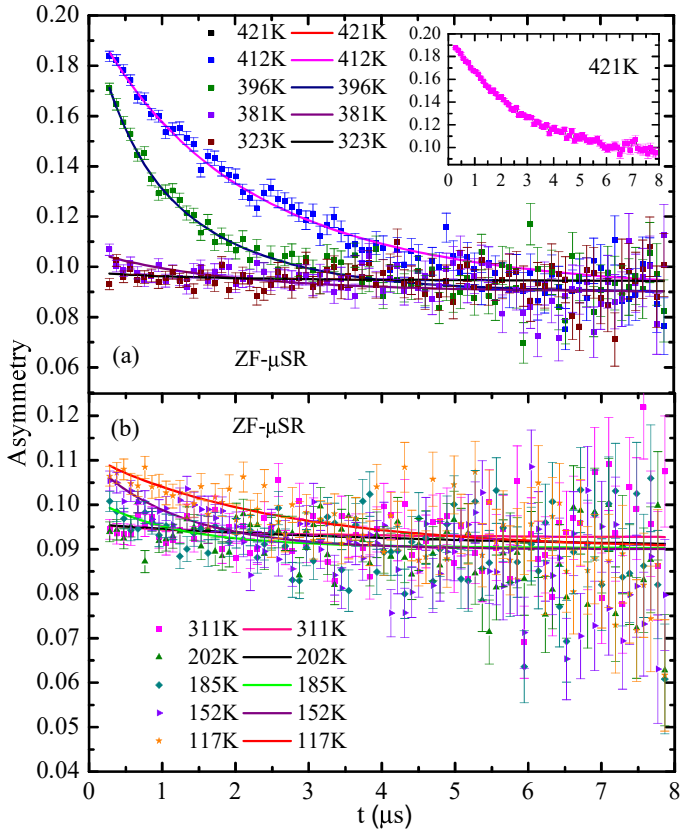


Figure 5.2: (a and b) The muon spin relaxation data measured in zero magnetic field (ZF) at various temperatures. The dotted curve depicts the observed data, and the lines indicate the calculated data. The inset displays the asymmetry data as a function of time at 421 K.

a function of time and this provides the information about the muon depolarization as a function of time. The muon polarization is measured as a function of time G(t) can be expressed as following equation [62]:

$$G(t) = \frac{B(t) - \alpha F(t)}{B(t) + \alpha F(t)} \tag{5.1}$$

Here, F(t) and B(t) represent the number of positrons detected at a given time t by the forward and backward detectors, respectively. It provides information about the local magnetization state. $\alpha$ is a correction factor for the detector, determined by the relative counting efficiency of the forward and backward detectors. Generally, muon relaxation asymmetry decay in magnetic materials follows a simple exponential relation, $G(t) = A_0 exp(-\lambda t) + bg$ [52], where $A_0$ is the initial asymmetry, and $\lambda$ is the muon spin relaxation rate. $bg$ represents the constant of the depolarization function, which arises

from muons stopping outside the sample or those not being depolarized. In the present $Ni_2Mn_{1.4}In_{0.6}$ alloy, the single relaxation function can not fit the muon asymmetry in the whole temperature range. Although the double exponential function is well suitable to fit the relaxing part of asymmetry and explain the data in the measured temperatures [62]. The double exponential function is as follows,

$$G(t) = A_{10}exp(-\lambda_1 t) + A_{20}exp(-\lambda_2 t) + bg \tag{5.2}$$

where $A_{10}$ and $A_{20}$ are the initial asymmetry of the relaxing part of asymmetry, $\lambda_1$ and $\lambda_2$ are the muon spin relaxation rates. Fig. 5.2 shows the asymmetry measured in polycrystalline $Ni_2Mn_{1.4}In_{0.6}$ at different representative temperatures during cooling in zero field measurement. At a high temperature of 421 K, the measured muon asymmetry ($G(t)$) exhibits an exponential decay over time, indicating a PM nature at elevated temperatures (inset of Fig. 5.2(a))[63]. The magnetic ordering transition can be manifested by the oscillating component of muon asymmetry data in the zero field. The frequency of oscillation changes with the magnitude of the internal field [64]. By determining the asymmetry line form of muon data that exhibits no oscillation in the zero field, the magnetic ordering transition is also explored [21, 65]. Fig. 5.2 clearly shows that as the temperature decreases, the shape of the asymmetry data changes. At 421 K, muon asymmetry decays exponentially, but at lower temperatures, the decay deviates from this exponential behavior, showing a rapid decay from the initial asymmetry. Additionally, the fast relaxing component decreases as the temperature is reduced (Fig. 5.2(a)) and reappears below 200 K (Fig. 5.2(b)). At lower temperatures, the baseline asymmetry converges nearly the same value.

To determine the magnetization state with temperature in the so-called PM gap regime, we modelled the time-dependent asymmetry plots at different temperatures using the double exponential function (Eq. 5.2) with background ($bg = 0.12$) using MATID software [66]. Modelling with a double exponential function shows good convergence in the whole temperature range with $A_{20} = 0.4A_{10}$. In Figs. 5.2(a,b), the solid dots are the experimental data, and the solid lines are the calculated data. The obtained values of asymmetry and

relaxation rate are plotted as a function of temperature in Figs. 5.3(a,b), providing information about the magnetization state. In Fig. 5.3(a), the asymmetry values are larger and nearly independent of temperature above ∼395 K, suggesting the PM nature of the high-temperature phase. As temperature decreases, the asymmetry value sharply decreases at the transition temperature, indicating a substantial decoupling of the muon spin-polarized state due to the internal field. The sharp change is due to the onset of the ordered spin state (i.e., due to the ordered magnetic moment) and the very narrow critical temperature regime of the transition. During the transition from a magnetically disordered state to a magnetically ordered state, there is typically an expected reduction of the relaxing component of asymmetry by $1/3$ in a powder or polycrystalline sample under ZF measurement. The remaining $2/3$ of the asymmetry will demonstrate time-dependent damped oscillations [60, 61]. In Fig. 5.3(a), the reduction in initial asymmetry ($A_{10}$) in the ordered state (be-

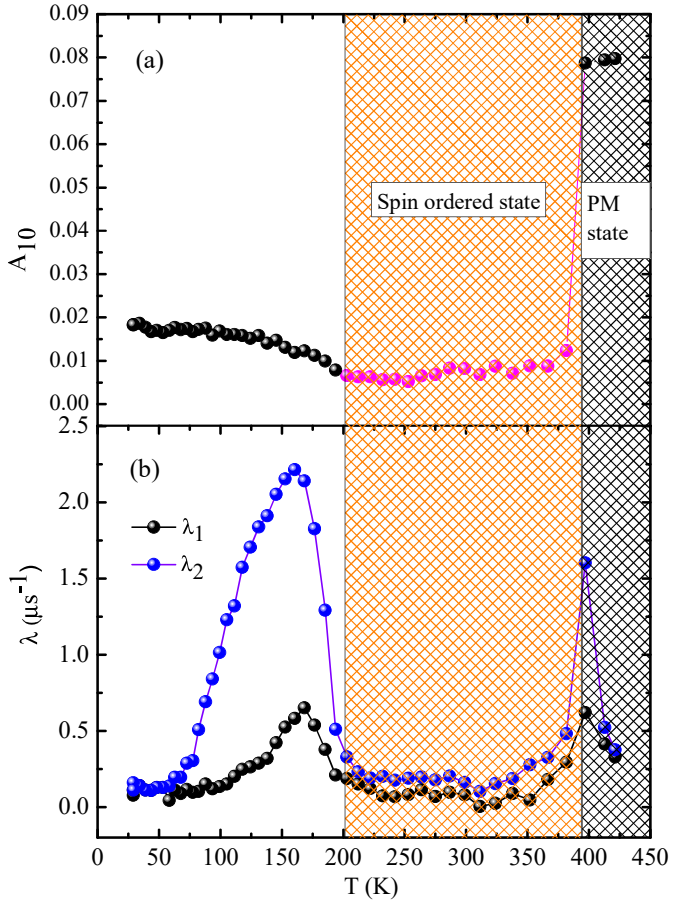


Figure 5.3: (a) The muon asymmetry $A_{10}$ measured as a function of temperature in zero magnetic field during the cooling process. (b) The temperature dependence of the muon depolarization rate $\lambda$ measured in zero magnetic field during cooling.

low $T_C$) is significantly less than the asymmetry observed in the high-temperature state. This disparity may be explained by the existence of a fast relaxing component. As the temperature decreases below $T_M$, the asymmetry value remains low, around $A_0 \sim 0.0065$, confirming the ordered nature of the magnetic moment even after the magneto structural transition. The absence of oscillations in the asymmetry data may be attributed to the significant local internal field at the muon implantation sites, resulting in a muon spin precession frequency that is too high to be detected by the instrument spectrometer [21, 61]. The magnetization sharply decreases below $T_M$ (Fig. 5.1), indicating a sudden loss of magnetic ordering due to the magneto-structural transition. As the temperature decreases further, the rise in magnetization within the martensite phase is referred to as the second magnetic transition ($T_C^M$). Therefore, the potential magnetization states in the so-called PM gap after the martensite transformation are (a) a disordered phase (either a pure PM phase or a PM phase with FM correlations) or (b) an ordered phase (either a pure AFM phase or an AFM phase with FM correlations). As seen in Fig. 5.3(a), the $A_{10}$ sharply decreases at lower values near the magnetic transition and remains nearly constant until the next magnetic transition temperature ($T_C^M$). This indicates the absence of any further spin-disordered state, meaning there is no PM phase or PM phase with FM correlation. This rules out the possibility of a disordered state below $T_M$, i.e., the case (a). Hence, the magnetization state below the $T_M$ is an ordered spin magnetized state. In the $M(T)$ plot, the magnetization in the so-called PM gap regime is slightly higher than in the higher-temperature PM phase, indicating that a pure AFM state is not present, indicating the coexistence of the AFM phase with FM correlation. The system undergoes a transition in its magnetic phase at $T_C$ (around 315 K) from a PM (disordered) phase to an FM (ordered) phase, as shown in the $M(T)$ plot (Fig. 5.1). However, the sharp decrease in asymmetry occurs around 395 K, suggesting that the disorder-to-order magnetic phase transition temperature differs between the magnetization measurement and the muon asymmetry data analysis. This difference may be due to the presence of an ordered FM state above $T_C$ or structural disorder, such as the presence of the martensite phase in the high-temperature austenite phase, which requires further investigation.

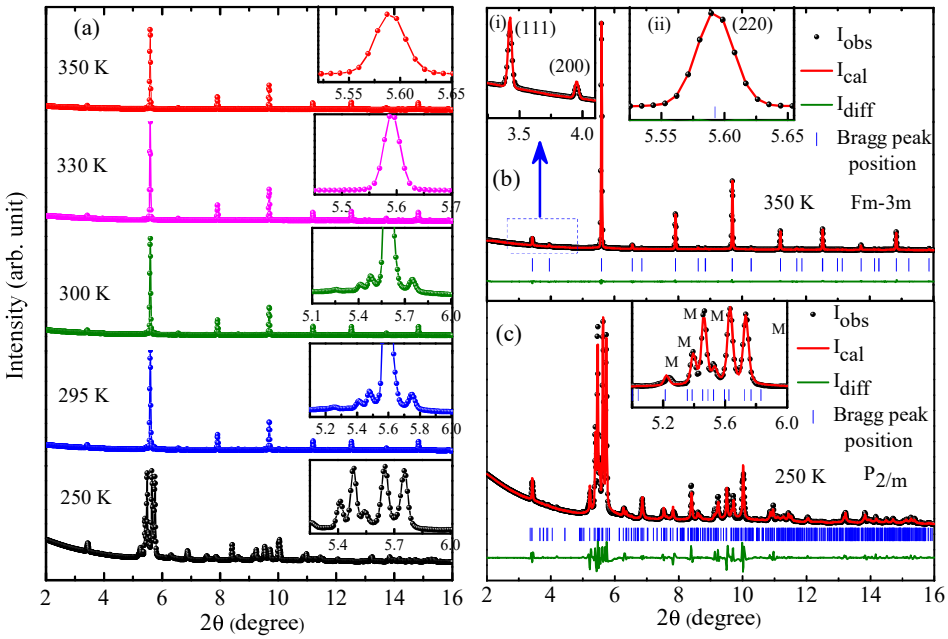


Figure 5.4: (a) Synchrotron X-ray powder diffraction (SXRPD) patterns of $Ni_2Mn_{1.4}In_{0.6}$ are shown at representative temperatures. Insets show a magnified view of the most intense peak at their respective temperatures (b) Le Bail refinement of the SXRPD pattern of $Ni_2Mn_{1.4}In_{0.6}$ in the austenite phase at 350 K. Inset (i) shows a magnified view of the (111) and (200) peaks, indicating $L2_1$ ordering. Inset (ii) shows the fitted most intense peak (220). (c) Le Bail refinement of SXRPD pattern of $Ni_2Mn_{1.4}In_{0.6}$ in the martensite phase at 250 K. The inset displays an enlarged view of the split main peak. The experimental peak profile is represented by black circles, while the calculated peak profile and the difference are shown by the red and green solid lines, respectively. The blue lines mark the positions of the Bragg peaks.

Hence, the magnetization state below the $T_C$ is an ordered spin magnetized state, i.e. coexistence of the AFM phase with FM correlation. Since the system changes its magnetic phase at the $T_C(\sim 315\,\mathrm{K})$ from the PM (disorder) phase to the FM (order) phase as shown in $M(T)$ (Fig. 5.1) but the sharp decrease in the asymmetry is around $\sim 395\,\mathrm{K}$, i.e. the disorder to order magnetic phase transition temperature is different in both magnetization measurement and muon asymmetry data analysis. The reason for this above transition temperature difference may be due to the presence of the ordered FM state above $T_C$ or structural disorder, i.e. the presence of the martensite phase in the high-temperature austenite phase, which needs to be further investigated. To investigate the information about the local structure, we performed the temperature-dependent PDF data analysis in the high-temperature cubic phase and a low-temperature martensite phase. The relaxation rate is plotted as a function of the temperature in Fig. 5.3(b). The relaxation rate sharply

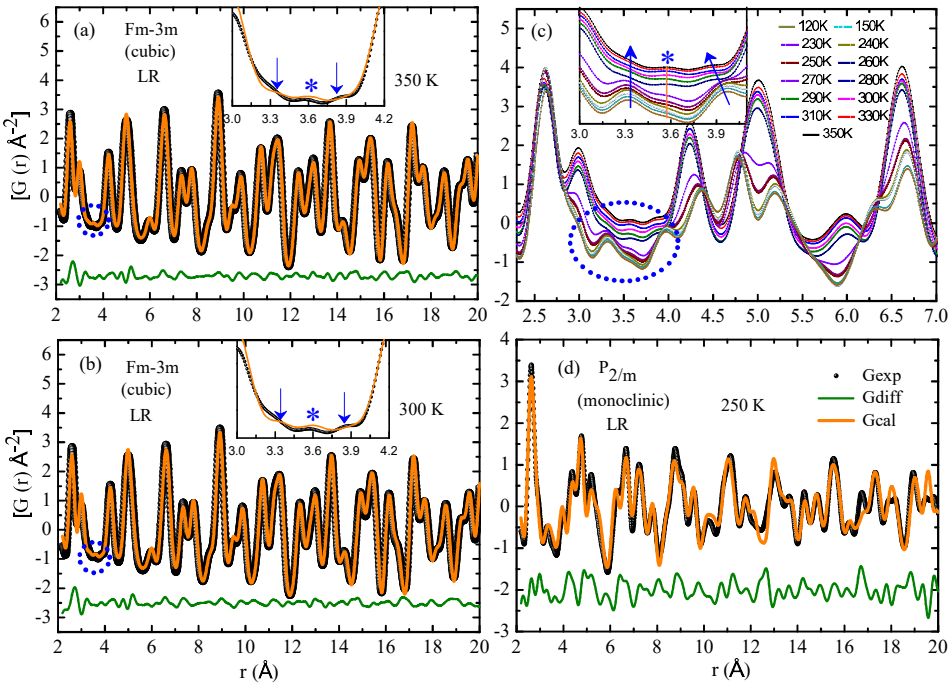


Figure 5.5: Real space Rietveld refinement of PDF data using space group $Fm\bar{3}m$ (a) at 350 K (b) at 300 K in long-range. Black dots represent the observed data points, the orange line indicates the calculated data points, and the green line indicates the difference between the observed and calculated data. The insets provide a zoomed view of the misfit peaks. (c) Temperature-dependent PDF data are plotted as a function of atomic pair distance in the temperature range 350 K to 120 K at representative temperatures. Insets show a zoomed view around the expected newly developed martensite peaks. (d) Real space Rietveld refined PDF data at 120 K using space group $P_{2/m}$ modulated structure.

increases at the $T_C$ because of the onset of the FM phase. The relaxation rate can be given by the equation $\lambda \propto \gamma_\mu^2 < B_\mu^2 > \tau$ where $< B_\mu^2 >$ is the thermal average of the fluctuating internal field, $\gamma_\mu$ is the gyromagnetic ratio of the muon ($2\pi 135.539$ MHz/T) and $\tau$ is the spin correlation time [50, 67]. Conventionally, near the magnetic phase transition, the correlation time becomes longer due to spins' critically slowing down phenomena. So, there is a sharp rise in the relaxation rate near the transition, and after getting the maximum value at its peak, it starts decreasing below the transition. This similar behaviour is also reflected in the relaxation rate vs temperature plot in Fig. 5.3(b). The sharp rise and decrease in $\lambda$ near transition temperature show a narrow critical transition regime. The observed peak is above the $T_C$, i.e. it also follows the asymmetry vs temperature plot. A broad peak is observed below $T_M$. This may be due to the magnetic frustration at the second magnetic transition, and it is also reflected in the asymmetry vs tempera-

ture plot as asymmetry values start increasing again $\sim$ 200 K. In Fig. 5.3(a), $A_{10}$ sharply decreases with the temperature at approximately 395 K, indicating a magnetic transition significantly above the $T_C$ of around 315 K, as shown in the $M(T)$ plot (Fig. 5.1). There are two possible explanations for the higher transition temperature observed in the muon data analysis: (i) ferromagnetic correlations may emerge at much higher temperatures, which are not detectable by standard magnetic measurements. This is due to the dynamic spin detection sensitivity range of a standard magnetometer, which spans from $10^{-2}$ Hz to $10^3$ Hz, compared to the muon spin relaxation spectroscopy's sensitivity range of $10^4$ Hz to $10^{12}$ Hz; (ii) there may be a different structural phase, along with the cubic phase, present at higher temperatures that also maintains a spin-ordered state. To determine the magnetic state above the $T_C$, we plotted the $1/\chi$ versus $T$, as shown in the inset (i) of Fig. 5.1. This plot was fitted using the Curie-Weiss equation $1/\chi = T/C - T_C/C$, and it was observed that $1/\chi$ is linear in the high-temperature range. The plot intersects the temperature axis at approximately 368 K, well above $T_C$. Therefore, it suggests that the ferromagnetic correlation developed much above the $T_C$ and above $T_C$ system is not in the pure PM phase. Thermal hysteresis is evident at the magnetic transition $T_C$ in the $M(T)$ plot. Inset (ii) of Fig. 5.1 shows the zoomed-in view of the thermal hysteresis around $T_C$. The origin of the hysteresis may be due to the presence of the local martensite phase within the cubic phase at high temperatures.

### 5.3.3 Temperature dependent synchrotron X-ray diffraction

To investigate the structural phase across the temperature range, we conducted temperature-dependent high-resolution SXRPD measurements. The high-resolution SXRPD data at selected temperatures (250 K, 295 K, 300 K, 330 K, and 350 K) are presented in Fig. 5.4(a), revealing structural changes with temperature.The insets of Fig. 5.4(a) provide a zoomed view of the most intense peaks in the corresponding X-ray diffraction patterns. Fig. 5.4(b) displays the Le Bail fit of the SXRPD data at 350 K, with all peaks accurately indexed using the $Fm\bar{3}m$ space group, indicating that the high-temperature phase is a single phase. The presence of the (111) and (200) peaks signifies $L2_1$ ordering (inset (i)). The refined lat-

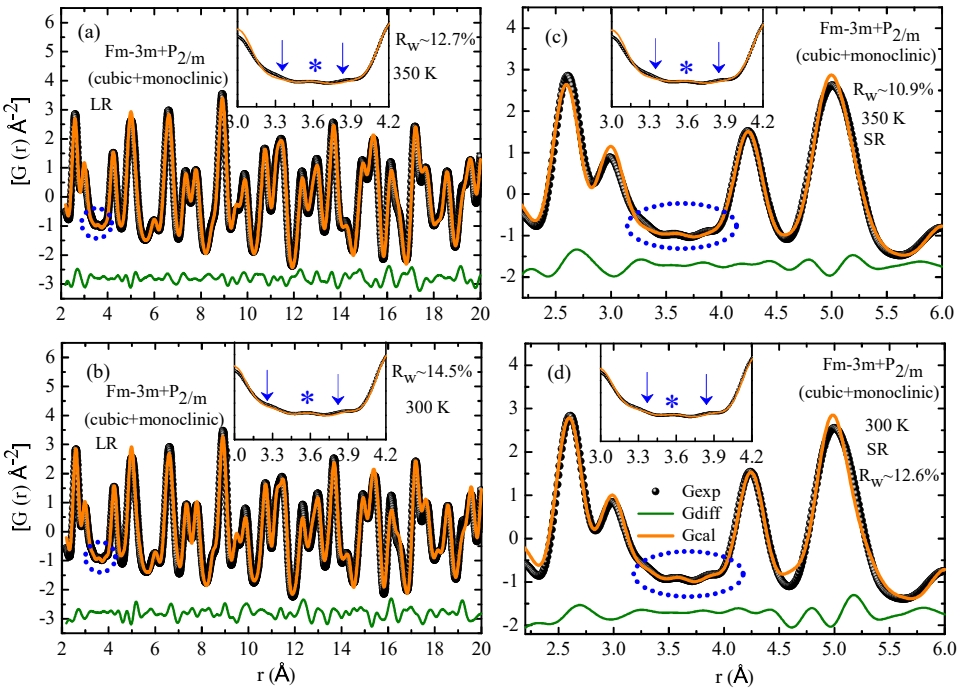


Figure 5.6: Figs (a) & (b) show the real space Rietveld double phase refined PDF data using space group $Fm\bar{3}m$ and $P_{2/m}$ at 350 K and 300 K in LR. Insets show the zoomed view of the unfitted peaks at 3.32 Å and 3.85 Å. Figs (c) & (d) show the real space Rietveld double phase refined PDF data using space group $Fm\bar{3}m$ and $P_{2/m}$ at 350 K and 300 K in SR. Insets show the zoomed view of the fitted peaks at 3.32 Å and 3.85 Å. Black dots represent the observed data points, the orange line indicates the calculated data points, and The green line indicates the difference between the observed and fitted plots

tice parameter is 6.0044(5) Å. From high to low temperatures (at $T_M$), the main cubic peak (220) splits into multiple peaks, which are expected martensite peaks. A zoomed view of these peaks is shown in the inset of Fig. 5.4(c). The Le Bail fit of the low-temperature (250 K) martensite phase is performed with monoclinic space group $P_{2/m}$ 3M (shown in Fig. 5.4(c)). The refined lattice parameters are $a$ =4.4324(3) Å, $b$ =5.8616(5) Å, $c$ =12.982(1) Å, $\beta$ =92.128(5)°. This confirms that the low-temperature phase is a monoclinic phase, and the high-temperature phase is purely cubic, with no evidence of the presence of martensite phase. X-ray diffraction measurements reveal only the long-range (LR) ordered crystal structure, so we also conducted temperature-dependent PDF analysis to detect any local structure in the long-range cubic austenite phase,

### 5.3.4 Temperature dependent pair distribution function analysis

In order to investigate the presence of the local structural phase in the high-temperature regime of the austenite phase, we performed the temperature-dependent PDF analysis. PDF analysis is based on the total scattering method, and it is sensitive to both Bragg and diffuse scattering, allowing it to determine long-range (LR) and short-range (SR) (local) structures, respectively [66, 68, 69]. The total scattering structure function ($G(r)$) was obtained from the high-resolution SXRPD data by standard normalization procedure and background correction using the program PDFgetx3 [70]. The peak position corresponds to the distance between atomic pairs, and the peak intensity depends on the number of pairs with the same interatomic distance and the scattering factors of the individual pairs. The real space Rietveld fitting was done using PDFFIT2 software [71]. Figs. 5.5(a,b) show the real space Rietveld refined plots in the long-range order at 350 K and 300 K, respectively. All peaks are well-fitted using the Fm-3m space group, with lattice parameters of 6.003(1) Å and 5.997(4) Å, respectively, except for peaks at 3.32 Å, 3.58 Å, and 3.85 Å (magnified views of these unfitted peaks are shown in the insets). These distances are also absent in the model PDF calculated using the lattice parameters. This suggests these peaks do not correspond to the Fm-3m space group. To study the behavior of the unfitted peaks with temperature, we plotted the temperature-dependent PDF data at representative temperatures ranging from 350 to 120 K, as shown in Fig. 5.5(c). It can be observed that the intensity of peaks at 3.32 Å and 3.85 Å increases as the temperature decreases (indicated by arrows in the inset). Therefore, from 350 K to low temperature, the increase in the intensity of peaks indicates the possibility of the presence of the martensite phase at high temperature, and it dominates as it completely transforms into the martensite phase. To determine the structure of the low-temperature phase using PDF data, we performed the real space Rietveld refinement at 250K with space group $P_{2/m}$ (Fig. 5.5(d)) The lattice parameter of the fitted monoclinic phase is $a$ =4.355(6) Å, $b$ =5.687(6) Å, $c$ =12.94(1) Å, and $\beta = 92.5(1)^\circ$ which is similar to the lattice parameter obtained using Le Bail refinement of the SXRPD data (Fig. 5.4(d)). Having this observation, we performed double phase (cubic phase with space group $Fm\bar{3}m$ and monoclinic phase with space group $P_{2/m}$ with

3M modulation) real space Rietveld refinement of the PDF data at 350 K as well as 300 K in the long-range (Figs. 5.6(a,b)). Again, the peaks at 3.32 Å and 3.85 Å positions remain unfit, and these distances are also not present in the modelled PDF using the parameters of both phases. Insets show the magnified view of the unfitted peaks. The corresponding lattice parameters are shown in Table 5.1. Now, we performed the real space Rietveld

Table 5.1: Lattice parameters obtained from the PDF refinement using cubic phase with space group $Fm\bar{3}m$ and monoclinic phase with space group $P_{2/m}$ with 3M modulation in the LR regime at 350 K and 300 K.

| Long-range refined | 350 K | 300 K |
|---|---|---|
| cubic | a=6.007(4)Å | a=6.001(3)Å |
| monoclinic | a=4.3737(3)Å<br>b=5.788(5)Å<br>c=12.978(6)Å<br>$\beta$=92.594(3)° | a=4.343(2)Å<br>b=5.681(2)Å<br>c=12.924(2)Å<br>$\beta$=92.28(2)° |

fit in SR with both phases at temperatures 350 K and 300 K as shown in Figs. 5.6(c,d)). Both peaks, which were previously unfitted, are now well-fitted. The model PDF shows the distances 3.32 Å and 3.91 Å, i.e. in the martensite phase, atomic pairs correspond to these distances. The corresponding lattice parameters are shown in Table 5.2. Hence, it is confirmed that the local martensite phase is present in the long-range cubic structure. There is no atomic pair present corresponding to the distance 3.58 Å in both the cubic as well as monoclinic phase (shown by the star in the inset of Fig. 5.5(c)). This may be due to the termination error [71] because it does not correspond to any physical atomic pair in the monoclinic and cubic phases. The wavelength of the peak at $r \sim 3.58$Å matches with the wavelength of the termination ripple $\lambda = 2\pi/\text{Qmax}$ [66], with Qmax$= 20.73$ Å$^{-1}$. This confirms that the PDF peak at $r \sim 3.58$ Å is due to termination error. Since the martensite phase is a minor phase and is locally present in the cubic phase. Therefore, it will not affect much magnetization, and the magnetic component of the austenite phase will be dominating up to the $T_M$. Hence, it can be concluded that in the asymmetry vs temperature plot, the shift in magnetic transition temperature at a higher temperature is due to the local structural disorder (martensite phase) in the austenite phase.

Table 5.2: Lattice parameters obtained from the PDF refinement using cubic phase with space group $Fm\bar{3}m$ and monoclinic phase with space group $P_{2/m}$ with 3M modulation in the SR regime at 350 K and 300 K.

| Short-range refined | 350 K | 300 K |
|---|---|---|
| cubic | a=6.007(3)Å | a=6.002(1)Å |
| monoclinic | a=4.3737(5)Å<br>b=5.788(5)Å<br>c=12.989(7)Å<br>$\beta$=92.59(4)° | a=4.359(4)Å<br>b=5.681(2)Å<br>c=12.942(1)Å<br>$\beta$=92.28(2)° |

## 5.4 Conclusion

This study explores the magnetic state within the PM gap region of the martensite phase in $Ni_2Mn_{1.4}In_{0.6}$ MSMA using the muon spin relaxation ($\mu$SR) technique. The observed asymmetry values remain constant and are higher at elevated temperatures, indicating the PM state of the high-temperature austenite phase. The sharp decline in observed asymmetry values with decreasing temperature signifies a transition from a disordered (PM) phase to an ordered magnetic phase. The lower asymmetry value remains almost constant until the magnetic transition temperature in the martensite phase, $T_C^M$. This indicates that the magnetization state of $Ni_2Mn_{1.4}In_{0.6}$ is an ordered magnetic phase below $T_M$, and not a PM phase. The small asymmetry values are observed even above $T_C$ ($\sim$315 K) due to the presence of the local martensite phase within the high-temperature regime of the austenite phase. This local martensite phase in the cubic structure may possess an ordered spin structure, which depolarizes the muon spin even above the $T_C$. This study provides a clear understanding of the magnetic state in the so-called PM gap regime and opens a way for investigating magnetic interactions in the modulated structural phase.

# References

[1] H. E. Karaca, I. Karaman, B. Basaran, Y. Ren, Y. I. Chumlyakov, and H. J. Maier, "Magnetic Field-Induced Phase Transformation in NiMnCoIn Magnetic Shape-Memory Alloys—A New Actuation Mechanism with Large Work Output," *Adv. Funct. Mater.*, vol. 19, no. 7, pp. 983–998, 2009.

[2] J. Liu, T. Gottschall, K. P. Skokov, J. D. Moore, and O. Gutfleisch, "Giant magnetocaloric effect driven by structural transitions," *Nat. Mater.*, vol. 11, no. 7, pp. 620–626, 2012.

[3] S. Zuo, F. Liang, Y. Zhang, L. Peng, J. Xiong, Y. Liu, R. Li, T. Zhao, J. Sun, F. Hu, *et al.*, "Zero-field skyrmions generated via premartensitic transition in $Ni_{50}Mn_{35.2}In_{14.8}$ alloy," *Phys. Rev. Mater.*, vol. 2, no. 10, p. 104408, 2018.

[4] R. Kainuma, Y. Imano, W. Ito, Y. Sutou, H. Morito, S. Okamoto, O. Kitakami, K. Oikawa, A. Fujita, T. Kanomata, *et al.*, "Magnetic-field-induced shape recovery by reverse phase transformation," *Nat.*, vol. 439, no. 7079, pp. 957–960, 2006.

[5] T. Krenke, E. Duman, M. Acet, E. F. Wassermann, X. Moya, L. Mañosa, and A. Planes, "Inverse magnetocaloric effect in ferromagnetic Ni-Mn-Sn alloys," *Nat. Mater.*, vol. 4, no. 6, pp. 450–454, 2005.

[6] S. Singh, L. Caron, S. W. D'Souza, T. Fichtner, G. Porcari, S. Fabbrici, C. Shekhar, S. Chadov, M. Solzi, and C. Felser, "Large Magnetization and Reversible Magnetocaloric Effect at the Second-Order Magnetic Transition in Heusler Materials," *Adv. Mater.*, vol. 28, no. 17, pp. 3321–3325, 2016.

[7] V. Sharma, M. Chattopadhyay, K. Shaeb, A. Chouhan, and S. Roy, "Large magnetoresistance in $Ni_{50}Mn_{34}In_{16}$ alloy," *Appl. Phys. Lett.*, vol. 89, no. 22, p. 222509, 2006.

[8] I. Dubenko, A. Pathak, S. Stadler, N. Ali, Y. Kovarskii, V. Prudnikov, N. Perov, and

A. Granovsky, "Giant Hall effect in Ni-Mn-In Heusler alloys," *Phys. Rev. B*, vol. 80, no. 9, p. 092408, 2009.

[9] A. Çakır, M. Acet, and M. Farle, "Exchange bias caused by field-induced spin reconfiguration in Ni-Mn-Sn," *Phys. Rev. B*, vol. 93, no. 9, p. 094411, 2016.

[10] M. Ye, A. Kimura, Y. Miura, M. Shirai, Y. Cui, K. Shimada, H. Namatame, M. Taniguchi, S. Ueda, K. Kobayashi, *et al.*, "Role of electronic structure in the martensitic phase transition of $Ni_2Mn_{1+x}Sn_{1-x}$ studied by hard-X-ray photoelectron spectroscopy and ab initio calculation," *Phys. Rev. Lett.*, vol. 104, no. 17, p. 176401, 2010.

[11] T. Krenke, M. Acet, E. F. Wassermann, X. Moya, L. Mañosa, and A. Planes, "Martensitic transitions and the nature of ferromagnetism in the austenitic and martensitic states of Ni-Mn-Sn alloys," *Phys. Rev. B*, vol. 72, no. 1, p. 014412, 2005.

[12] S. Chatterjee, S. Giri, S. Majumdar, A. Deb, S. De, and V. Hardy, "Magneto-structural instability in $Ni_2Mn_{1.4}Sb_{0.6}$ alloy," *J. Condens. Matter Phys.*, vol. 19, no. 34, p. 346213, 2007.

[13] K. Priolkar, P. Bhobe, D. Lobo, S. D'Souza, S. Barman, A. Chakrabarti, and S. Emura, "Antiferromagnetic exchange interactions in the $Ni_2Mn_{1.4}In_{0.6}$ ferromagnetic Heusler alloy," *Phys. Rev. B*, vol. 87, no. 14, p. 144412, 2013.

[14] P. Bhobe, K. Priolkar, and A. Nigam, "Anomalous magnetic properties in $Ni_{50}Mn_{35}In_{15}$," *J. Phys. D Appl. Phys.*, vol. 41, no. 23, p. 235006, 2008.

[15] S. Fabbrici, F. Albertini, A. Paoluzi, F. Bolzoni, R. Cabassi, M. Solzi, L. Righi, and G. Calestani, "Reverse magnetostructural transformation in Co-doped NiMnGa multifunctional alloys," *Appl. Phys. Lett.*, vol. 95, no. 2, p. 022508, 2009.

[16] T. Kihara, T. Roy, X. Xu, A. Miyake, M. Tsujikawa, H. Mitamura, M. Tokunaga, Y. Adachi, T. Eto, and T. Kanomata, "Observation of inverse magnetocaloric effect in magnetic-field-induced austenite phase of Heusler alloys $Ni_{50-x}Co_xMn_{31.5}Ga_{18.5}$ (x=9 and 9.7)," *Phys. Rev. Mater.*, vol. 5, no. 3, p. 034416, 2021.

[17] S. Aksoy, M. Acet, P. Deen, L. Mañosa, and A. Planes, "Magnetic correlations in martensitic Ni-Mn-based Heusler shape-memory alloys: Neutron polarization analysis," *Phys. Rev. B*, vol. 79, no. 21, p. 212401, 2009.

[18] F. Orlandi, S. Fabbrici, F. Albertini, P. Manuel, D. Khalyavin, and L. Righi, "Long-range antiferromagnetic interactions in Ni-Co-Mn-Ga metamagnetic Heusler alloys: A two-step ordering studied by neutron diffraction," *Phys. Rev. B*, vol. 94, no. 14, p. 140409, 2016.

[19] S. Fabbrici, J. Kamarad, Z. Arnold, F. Casoli, A. Paoluzi, F. Bolzoni, R. Cabassi, M. Solzi, G. Porcari, C. Pernechele, *et al.*, "From direct to inverse giant magnetocaloric effect in Co-doped NiMnGa multifunctional alloys," *Acta Mater.*, vol. 59, no. 1, pp. 412–419, 2011.

[20] S. K. Sarkar, S. Ahlawat, S. D. Kaushik, P. Babu, D. Sen, D. Honecker, and A. Biswas, "Magnetic ordering of the martensite phase in Ni-Co-Mn-Sn-based ferromagnetic shape memory alloys," *J. Condens. Matter Phys.*, vol. 32, no. 11, p. 115801, 2019.

[21] J. Sannigrahi, S. Pramanick, S. Chatterjee, J. Lord, D. Khalyavin, A. Hillier, D. Adroja, and S. Majumdar, "Magnetic states of Ni-Mn-Sn based shape memory alloy: a combined muon spin relaxation and neutron diffraction study," *Phys. Rev. B*, vol. 99, no. 22, p. 224401, 2019.

[22] X. Moya, D. González-Alonso, L. Mañosa, A. Planes, V. Garlea, T. Lograsso, D. Schlagel, J. Zarestky, S. Aksoy, and M. Acet, "Lattice dynamics in magnetic superelastic Ni-Mn-In alloys: Neutron scattering and ultrasonic experiments," *Phys. Rev. B*, vol. 79, no. 21, p. 214118, 2009.

[23] Z. Li, C. Jing, H. Zhang, D. Yu, L. Chen, B. Kang, S. Cao, and J. Zhang, "A large and reproducible metamagnetic shape memory effect in polycrystalline $Ni_{45}Co_5Mn_{37}In_{13}$ Heusler alloy," *J. Appl. Phys.*, vol. 108, no. 11, p. 113908, 2010.

[24] V. Buchelnikov, P. Entel, S. Taskaev, V. Sokolovskiy, A. Hucht, M. Ogura, H. Akai,

M. Gruner, and S. Nayak, "Monte Carlo study of the influence of antiferromagnetic exchange interactions on the phase transitions of ferromagnetic Ni-Mn-X alloys (X= In, Sn, Sb)," *Phys. Rev. B*, vol. 78, no. 18, p. 184427, 2008.

[25] C.-M. Li, Q.-M. Hu, R. Yang, B. Johansson, and L. Vitos, "Theoretical investigation of the magnetic and structural transitions of Ni-Co-Mn-Sn metamagnetic shape-memory alloys," *Phys. Rev. B*, vol. 92, no. 2, p. 024105, 2015.

[26] C. Tan, Y. Huang, X. Tian, J. Jiang, and W. Cai, "Origin of magnetic properties and martensitic transformation of Ni-Mn-In magnetic shape memory alloys," *Appl. Phys. Lett.*, vol. 100, no. 13, p. 132402, 2012.

[27] V. Sokolovskiy, V. Buchelnikov, M. Zagrebin, P. Entel, S. Sahoo, and M. Ogura, "First-principles investigation of chemical and structural disorder in magnetic $Ni_2Mn_{1+x}Sn_{1-x}$ Heusler alloys," *Phys. Rev. B*, vol. 86, no. 13, p. 134418, 2012.

[28] V. Sokolovskiy, A. Grünebohm, V. Buchelnikov, and P. Entel, "Ab initio and monte carlo approaches for the magnetocaloric effect in Co-and In-doped Ni-Mn-Ga Heusler alloys," *Entropy*, vol. 16, no. 9, pp. 4992–5019, 2014.

[29] M. Khan, I. Dubenko, S. Stadler, and N. Ali, "Magnetostructural phase transitions in $Ni_{50}Mn_{25+x}Sb_{25-x}$ Heusler alloys," *J. Condens. Matter Phys.*, vol. 20, no. 23, p. 235204, 2008.

[30] S. Pandey, A. Quetz, I. Rodionov, A. Aryal, M. Blinov, I. Titov, V. Prudnikov, A. Granovsky, I. Dubenko, S. Stadler, *et al.*, "Magnetic, transport, and magnetocaloric properties of boron doped Ni-Mn-In alloys," *J. Appl. Phys.*, vol. 117, no. 18, p. 183905, 2015.

[31] B. Wang, Y. Liu, L. Wang, S. Huang, Y. Zhao, Y. Yang, and H. Zhang, "Exchange bias and its training effect in the martensitic state of bulk polycrystalline $Ni_{49.5}Mn_{34.5}In_{16}$," *J. Appl. Phys.*, vol. 104, no. 4, p. 043916, 2008.

[32] M. Blinov, A. Aryal, S. Pandey, I. Dubenko, S. Talapatra, V. Prudnikov, E. Lähderanta, S. Stadler, V. Buchelnikov, V. Sokolovskiy, *et al.*, "Effects of magnetic and

structural phase transitions on the normal and anomalous Hall effects in Ni-Mn-In-B Heusler alloys," *Phys. Rev. B*, vol. 101, no. 9, p. 094423, 2020.

[33] Z. Li, S. Dong, Z. Li, B. Yang, F. Liu, C. Sánchez-Valdés, J. S. Llamazares, Y. Zhang, C. Esling, X. Zhao, *et al.*, "Giant low-field magnetocaloric effect in Si alloyed Ni-Co-Mn-In alloys," *Scr. Mater.*, vol. 159, pp. 113–118, 2019.

[34] R. Umetsu, R. Kainuma, Y. Amako, Y. Taniguchi, T. Kanomata, K. Fukushima, A. Fujita, K. Oikawa, and K. Ishida, "Mössbauer study on martensite phase in $Ni_{50}Mn_{36.5}Fe_{0.557}Sn_{13}$ metamagnetic shape memory alloy," *Appl. Phys. Lett.*, vol. 93, no. 4, p. 042509, 2008.

[35] V. Khovaylo, T. Kanomata, T. Tanaka, M. Nakashima, Y. Amako, R. Kainuma, R. Umetsu, H. Morito, and H. Miki, "Magnetic properties of $Ni_{50}Mn_{34.8}In_{15.2}$ probed by Mössbauer spectroscopy," *Phys. Rev. B*, vol. 80, no. 14, p. 144409, 2009.

[36] L. Mañosa, D. González-Alonso, A. Planes, E. Bonnot, M. Barrio, J.-L. Tamarit, S. Aksoy, and M. Acet, "Giant solid-state barocaloric effect in the Ni-Mn-In magnetic shape-memory alloy," *Nat. Mater.*, vol. 9, no. 6, pp. 478–481, 2010.

[37] F. Liu, Q. Wang, W. Ao, Y. Yu, L. Pan, and J. Li, "Magnetocaloric effect in high Ni content $Ni_{52}Mn_{48-x}In_x$ alloys under low field change," *J. Magn. Magn. Mater.*, vol. 324, no. 4, pp. 514–518, 2012.

[38] J. Liu, X. You, B. Huang, I. Batashev, M. Maschek, Y. Gong, X. Miao, F. Xu, N. van Dijk, and E. Brück, "Reversible low-field magnetocaloric effect in Ni-Mn-In-based Heusler alloys," *Phys. Rev. Mater.*, vol. 3, no. 8, p. 084409, 2019.

[39] B. Lu and J. Liu, "Elastocaloric effect and superelastic stability in Ni-Mn-In-Co polycrystalline Heusler alloys: hysteresis and strain-rate effects," *Sci. Rep.*, vol. 7, no. 1, pp. 1–11, 2017.

[40] T. Krenke, E. Duman, M. Acet, E. F. Wassermann, X. Moya, L. Mañosa, A. Planes, E. Suard, and B. Ouladdiaf, "Magnetic superelasticity and inverse magnetocaloric effect in Ni-Mn-In," *Phys. Rev. B*, vol. 75, no. 10, p. 104414, 2007.

[41] P. Yanda, L. Noohinejad, N. Mao, N. Peshcherenko, K. Imasato, A. K. Srivastava, Y. Guan, B. Giri, A. K. Sharma, K. Manna, *et al.*, "Giant Topological Hall Effect and Colossal Magnetoresistance in Heusler Ferromagnet near Room Temperature," *Adv. Mater.*, p. 2411240, 2024.

[42] B. Wang, Y. Liu, P. Ren, B. Xia, K. Ruan, J. Yi, J. Ding, X. Li, and L. Wang, "Large exchange bias after zero-field cooling from an unmagnetized state," *Phys. Rev. Lett.*, vol. 106, no. 7, p. 077203, 2011.

[43] X. Moya, L. Mañosa, A. Planes, S. Aksoy, M. Acet, E. F. Wassermann, and T. Krenke, "Cooling and heating by adiabatic magnetization in the $Ni_{50}Mn_{34}In_{16}$ magnetic shape-memory alloy," *Phys. Rev. B*, vol. 75, no. 18, p. 184412, 2007.

[44] P. Devi, S. Singh, B. Dutta, K. Manna, S. W. D'Souza, Y. Ikeda, E. Suard, V. Petricek, P. Simon, P. Werner, *et al.*, "Adaptive modulation in the $Ni_2Mn_{1.4}In_{0.6}$ magnetic shape-memory Heusler alloy," *Phys. Rev. B*, vol. 97, no. 22, p. 224102, 2018.

[45] K. K. Dubey, P. Devi, A. K. Singh, and S. Singh, "Improved crystallographic compatibility and magnetocaloric reversibility in Pt substituted $Ni_2Mn_{1.4}In_{0.6}$ magnetic shape memory Heusler alloy," *J. Magn. Magn. Mater.*, vol. 507, p. 166818, 2020.

[46] P. Brown, A. Gandy, R. Kainuma, T. Kanomata, K. Neumann, K. Oikawa, B. Ouladdiaf, A. Sheikh, and K. Ziebeck, "The field and temperature dependence of the magnetic and structural properties of the shape memory compound $Ni_{1.84}Mn_{1.64}In_{0.52}$," *J. Condens. Matter Phys.*, vol. 23, no. 45, p. 456004, 2011.

[47] P. Brown, A. Gandy, K. Ishida, R. Kainuma, T. Kanomata, K. Neumann, K. Oikawa, B. Ouladdiaf, and K. Ziebeck, "The magnetic and structural properties of the magnetic shape memory compound $Ni_2Mn_{1.44}Sn_{0.56}$," *J. Condens. Matter Phys.*, vol. 18, no. 7, p. 2249, 2006.

[48] P. Brown, A. Gandy, K. Ishida, W. Ito, R. Kainuma, T. Kanomata, K. Neumann, K. Oikawa, B. Ouladdiaf, A. Sheikh, *et al.*, "Magnetic and structural properties of

the magnetic shape memory compound $Ni_2Mn_{1.48}Sb_{0.52}$," *J. Condens. Matter Phys.*, vol. 22, no. 9, p. 096002, 2010.

[49] Y. Wei, X. Ma, Z. Feng, D. Adroja, A. Hillier, P. Biswas, A. Senyshyn, A. Hoser, J.-W. Mei, Z. Y. Meng, *et al.*, "Magnetic Phase Diagram of $Cu_{4-x}Zn_x(OH)_6FBr$ Studied by Neutron-Diffraction and $\mu$SR Techniques," *Chin. Phys. Lett.*, vol. 37, no. 10, p. 107503, 2020.

[50] C. Bonilla, N. Marcano, J. Herrero-Albillos, A. Maisuradze, L. García, and F. Bartolomé, "$\mu$SR study of short-range magnetic order in the paramagnetic regime of $ErCo_2$," *Phys. Rev. B*, vol. 84, no. 18, p. 184425, 2011.

[51] I. Gat-Malureanu, J. Carlo, T. Goko, A. Fukaya, T. Ito, P. Kyriakou, M. Larkin, G. Luke, P. Russo, A. Savici, *et al.*, "Muon spin relaxation and susceptibility measurements of an itinerant-electron system $Sr_{(1-x)}Ca_xRuO_3$: quantum evolution from ferromagnet to paramagnet," *Phys. Rev. B*, vol. 84, no. 22, p. 224415, 2011.

[52] M. Wilson, T. Hicken, M. Gomilšek, A. Štefančič, G. Balakrishnan, J. Loudon, A. Twitchett-Harrison, F. Pratt, M. Telling, and T. Lancaster, "Spin dynamics in bulk MnNiGa and $Mn_{1.4}Pt_{0.9}Pd_{0.1}Sn$ investigated by muon spin relaxation," *Phys. Rev. B*, vol. 104, no. 13, p. 134414, 2021.

[53] F.-X. Hu, B.-G. Shen, and J.-R. Sun, "Magnetic entropy change in $Ni_{51.5}Mn_{22.7}Ga_{25.8}$ alloy," *Appl. Phys. Lett.*, vol. 76, no. 23, pp. 3460–3462, 2000.

[54] S. Singh, R. Rawat, and S. Barman, "Existence of modulated structure and negative magnetoresistance in Ga excess Ni-Mn-Ga," *Appl. Phys. Lett.*, vol. 99, no. 2, p. 021902, 2011.

[55] W. Wang, Z. Liu, J. Zhang, J. Chen, G. Wu, W. Zhan, T. Chin, G. Wen, and X. Zhang, "Thermoelastic intermartensitic transformation and its internal stress dependency in $Ni_{52}Mn_{24}Ga_{24}$ single crystals," *Phys. Rev. B*, vol. 66, no. 5, p. 052411, 2002.

[56] S. Singh, P. Kushwaha, F. Scheibel, H.-P. Liermann, S. Barman, M. Acet, C. Felser, and D. Pandey, "Residual stress induced stabilization of martensite phase and its

effect on the magnetostructural transition in Mn-rich Ni-Mn-In/Ga magnetic shape-memory alloys," *Phys. Rev. B*, vol. 92, no. 2, p. 020105, 2015.

[57] R. Ranjan, S. Singh, H. Boysen, D. Trots, S. Banik, A. Awasthi, P. Mukhopadhyay, and S. Barman, "Competing tetragonal and monoclinic phases in $Ni_{2.2}Mn_{0.80}Ga$," *J. Appl. Phys.*, vol. 106, no. 3, p. 033510, 2009.

[58] L. C. Chapon, P. Manuel, P. G. Radaelli, C. Benson, L. Perrott, S. Ansell, N. J. Rhodes, D. Raspino, D. Duxbury, E. Spill, *et al.*, "Wish: The new powder and single crystal magnetic diffractometer on the second target station," *Neutron News*, vol. 22, no. 2, pp. 22–25, 2011.

[59] J. Brewer, "Advances in muon spin rotation," 1978.

[60] D. Ryan, J. Van Lierop, and J. Cadogan, "Zero-field muon spin relaxation studies of frustrated magnets: physics and analysis issues," *J. Condens. Matter Phys.*, vol. 16, no. 40, p. S4619, 2004.

[61] P. D. De Reotier and A. Yaouanc, "Muon spin rotation and relaxation in magnetic materials," *J. Condens. Matter Phys.*, vol. 9, no. 43, p. 9113, 1997.

[62] M. Hiroi, T. Hisamatsu, T. Suzuki, K. Ohishi, Y. Ishii, and I. Watanabe, "Muon spin relaxation study of spin-glass freezing in the Heusler compound $Ru_{1.9}Fe_{0.1}CrSi$," *Phys. Rev. B*, vol. 88, no. 2, p. 024409, 2013.

[63] H. Guo, K. Manna, H. Luetkens, M. Hoelzel, and A. Komarek, "Spin glass behavior in $LaCo_{1-x}Rh_xO_3$ (x=0.4,0.5,and 0.6)," *Phys. Rev. B*, vol. 94, no. 20, p. 205128, 2016.

[64] F. Pratt, "Field dependence of $\mu$SR signals in a polycrystalline magnet," *J. Condens. Matter Phys.*, vol. 19, no. 45, p. 456207, 2007.

[65] L. Clark, G. Sala, D. D. Maharaj, M. B. Stone, K. S. Knight, M. T. Telling, X. Wang, X. Xu, J. Kim, Y. Li, *et al.*, "Two-dimensional spin liquid behaviour in the triangular-honeycomb antiferromagnet $TbInO_3$," *Nat. Phys.*, vol. 15, no. 3, pp. 262–268, 2019.

[66] T. Egami and S. J. Billinge, "Underneath the Bragg Peaks: Structural Analysis of Complex Materials," *Elsevier, Pergamon*, 2003.

[67] R. Heffner, J. Sonier, D. MacLaughlin, G. Nieuwenhuys, G. Luke, Y. Uemura, I. William Ratcliff, S. Cheong, and G. Balakrishnan, "Muon spin relaxation study of $La_{(1-x)}Ca_xMnO_3$," *Phys. Rev. B*, vol. 63, no. 9, p. 094408, 2001.

[68] V. Petkov, "Pair distribution functions analysis," *Mater. Charact.*, vol. 1361, 2012.

[69] I.-K. Jeong, T. Darling, J. Lee, T. Proffen, R. Heffner, J. Park, K. Hong, W. Dmowski, and T. Egami, "Direct observation of the formation of polar nanoregions in $Pb(Mg_{1/3}Nb_{2/3})O_3$ using neutron pair distribution function analysis," *Phys. Rev. Lett.*, vol. 94, no. 14, p. 147602, 2005.

[70] P. Juhás, T. Davis, C. L. Farrow, and S. J. Billinge, "PDFget$X_3$: a rapid and highly automatable program for processing powder diffraction data into total scattering pair distribution functions," *J. Appl. Crystallogr.*, vol. 46, no. 2, pp. 560–566, 2013.

[71] C. Farrow, P. Juhas, J. Liu, D. Bryndin, E. Božin, J. Bloch, T. Proffen, and S. Billinge, "PDFfit2 and PDFgui: computer programs for studying nanostructure in crystals," *J. Condens. Matter Phys.*, vol. 19, no. 33, p. 335219, 2007.